

# Imine-Based Conjugated Polymers as High-Performance Organic Cathodes for Rechargeable Magnesium Batteries: Insights from Electronic Structure Design

Donggang Tao, Yudi Tang, Hongda Gui, Yuliang Cao, and Fei Xu\*

Rechargeable Mg batteries (RMBs) face challenges of cathode materials due to the high charge density of  $Mg^{2+}$  cations. Organic conjugated polymers, with tunable structures and flexible frameworks, offer promising selections for Mg-storage cathodes. This study compares three nitrogen-based conjugated polymers, polypyrrole (PPy, amine-rich), polyaniline (PANI, mixed amine/imine), and poly(*o*-phenylenediamine) (PoPD, imine-rich), to elucidate the advantageous nitrogen-based Mg-storage active sites and corresponding materials. Theoretical calculations reveal that PANI and PoPD exhibit lower LUMO energy levels and their imine ( $=N-$ ) groups show localized negative electrostatic potential

(ESP), favoring  $Mg^{2+}$  association via n-type redox reactions, unlike p-type amine ( $-NH-$ ) groups in PPy. PoPD, with dual imine groups and extended  $\pi$ -conjugation, demonstrates superior Mg-storage performance: a high initial capacity of  $208 \text{ mAh g}^{-1}$  ( $0.1 \text{ A g}^{-1}$ ), exceptional rate capability ( $72 \text{ mAh g}^{-1}$  at  $5 \text{ A g}^{-1}$ ), and long-term stability (81.75% retention after 1200 cycles). Mechanism analyses confirm  $Mg^{2+}/MgCl^+$  costorage via  $-N-$  coordination, facilitated by charge delocalization and flexible polymer chains. The work establishes imine-rich conjugated polymers as high-performance organic cathodes, highlighting structure–property relationships for advancing RMBs.

## 1. Introduction

The extensive utilization of renewable energy sources, represented by solar and wind power, has driven a rapidly growing demand for large-scale energy storage technologies with high safety and long lifespan.<sup>[1,2]</sup> Rechargeable Mg batteries (RMBs) are considered promising candidates for stationary energy storage due to the natural abundance, inherent safety and high theoretical volumetric capacity of Mg metal anodes.<sup>[3–5]</sup> However, compared with the recent progress of  $Mg^{2+}$  electrolytes, the shortage of cathode materials has severely hindered the development of RMBs.<sup>[6–10]</sup> The challenges of Mg-storage cathode design mainly originate from the intrinsic properties of  $Mg^{2+}$  cations.<sup>[11]</sup> With an ionic radius of only  $0.72 \text{ \AA}$  (smaller than the  $0.76 \text{ \AA}$  of  $Li^+$ ) but carrying a divalent positive charge,  $Mg^{2+}$  exhibits high charge density and strong polarization effects.<sup>[12,13]</sup> This results in strong interactions between  $Mg^{2+}$  and the negatively charged regions of cathode materials, leading to the low reversibility of Mg-storage reactions and sluggish  $Mg^{2+}$  diffusion kinetics.<sup>[14]</sup> As a result,

conventional inorganic RMB cathodes usually suffer from significantly inferior performance.<sup>[15]</sup>

Compared with inorganic materials, organic materials have distinct advantages including abundant resource availability, environmental friendliness, renewability, and tunable structures, which are considered ideal materials for RMB cathodes.<sup>[16]</sup> However, small molecular organic materials are facing the challenge of inevitable dissolution in electrolytes, whereas polymerization has been identified as an effective strategy to suppress the dissolution.<sup>[17]</sup> Organic conjugated polymers with extended  $\pi$ -conjugated structures have open chemical frameworks and electronic delocalization properties.<sup>[18]</sup> During Mg-storage reactions, conjugated polymers primarily undergo overall redox processes while facilitating charge delocalization through their conjugated systems.<sup>[19]</sup> This Mg-storage mechanism enhances reaction reversibility and ensures structural stability.<sup>[20]</sup> Additionally, organic conjugated polymers exhibit flexible and amorphous structural characteristics, which enable rapid  $Mg^{2+}$  diffusion by circumventing the limitations of inorganic crystalline lattices, while effectively mitigating mechanical stress during circulation.<sup>[21]</sup>

The design of organic RMB cathodes depends on the selection of electroactive functional groups coupled with appropriate conjugated architectures.<sup>[22]</sup> Previous research on organic Mg-storage cathodes mainly focused on polymers with oxygen-based coordinating atoms like conjugated carbonyl polymers.<sup>[23]</sup> In contrast, nitrogen-based conjugated polymer demonstrates comparable potential. The lower electronegativity of N atoms enables more reversible association/dissociation with  $Mg^{2+}$  cations, enhancing the Mg-storage reaction reversibility.<sup>[24]</sup> Representative N-based electroactive groups include amine ( $-NH-$ ) and imine ( $=N-$ ). To elucidate the Mg-storage characteristics of these two typical electroactive N-based groups and their corresponding polymers,

D. Tao, Y. Tang, H. Gui, F. Xu  
Key Laboratory of Hydraulic Machinery Transients  
Ministry of Education  
School of Power and Mechanical Engineering  
Wuhan University  
Wuhan 430072, China  
E-mail: xufei2058@whu.edu.cn

Y. Cao  
Hubei Key Lab of Electrochemical Power Sources  
College of Chemistry & Molecular Science  
Wuhan University  
Wuhan 430072, China

 Supporting information for this article is available on the WWW under <https://doi.org/10.1002/batt.202500226>

the present study systematically investigates three N-based conjugated polymers (**Figure 1a**): polypyrrole (PPy), polyaniline (PANI), and poly(o-phenylenediamine) (PoPD). Comparative analysis reveals that imine (=N—) groups with n-type redox reactions are more favorable as Mg-storage active sites compared to amine groups (—NH—) which undergo p-type reactions. As a nitrogen-rich polymer featuring dual imine groups and extended  $\pi$ -conjugated structures, PoPD provides abundant association sites for Mg storage owing to its phenazine units. These sites exhibit redox mechanisms analogous to carbonyl groups ( $C=N/C-N^-$  vs.  $C=O/C-O^-$ ) while delivering a high theoretical capacity. PoPD demonstrates excellent electrochemical performance with high initial specific capacity ( $208 \text{ mAh g}^{-1}$  at  $0.1 \text{ A g}^{-1}$ ), superior rate capability ( $72 \text{ mAh g}^{-1}$  at  $5 \text{ A g}^{-1}$ ), and long lifespan (81.75% capacity retention after 1200 cycles at  $5 \text{ A g}^{-1}$ ). This comparative study establishes the relationships between the structure of N-based conjugated polymers and their electrochemical Mg-storage behaviors, providing insights for developing high-performance organic RMB cathode materials.

## 2. Result and Discussion

Theoretical computation was first conducted for the three representative N-based conjugated polymers of PPy, PANI, and PoPD and the results are shown in Figure 1. All three conjugated polymers exhibit linear chain structures with extended  $\pi$ -conjugation, but are different in the connection methods. PPy is linked by  $\alpha$ -carbon between pyrrole units, where nitrogen exists as amine groups (—NH—). PANI adopts alternating connections between

amine (—NH—) and imine (=N—) units when bridging benzene rings.<sup>[25]</sup> In contrast, the polymerization process of PoPD has shown complexity due to two adjacent amine groups, which initially form a dimer of o-phenylenediamine (2,3-diaminophenazine) before undergoing chain elongation.<sup>[26,27]</sup> The high-temperature synthesis would inevitably induce partial oxidation of amino groups (—NH<sub>2</sub>) into —OH or C=O (denoted as X in Figure 1a).<sup>[28]</sup> Molecular electrostatic potential (MESP) derived from theoretical calculations (Figure 1b) shows that —NH— regions consistently show strongly positive ESP values, which could hardly be the Mg-association site. Meanwhile, negative potential regions are primarily localized on the =N— groups in PANI and PoPD, which originates from the presence of lone pair electrons in =N—. The MESP analysis indicates that =N— is more likely to be the association site for the Mg<sup>2+</sup> compared to —NH—.

Further, frontier molecular orbital analysis has shown the electronic structure differences (Figure 1c). PPy exhibits a high lowest unoccupied molecular orbital (LUMO) energy level of  $-0.87 \text{ eV}$ , indicating the limitation of electron acceptance because of the high electron density in pyrrole rings. This electronic structure explains the p-type redox behavior of PPy accompanied by anion coordination during electrochemical cycling. In contrast, PANI and PoPD demonstrate much lower LUMO energy levels of  $-2.87$  and  $-2.53 \text{ eV}$ , respectively, with the LUMO orbitals predominantly localized on imine (=N—) groups and adjacent aromatic rings, indicating the n-type electrochemical reaction active centers suitable for Mg association.<sup>[19]</sup> The favorable Mg-storage potential of PoPD originates from a larger number of n-type active sites (=N—). Electron localization function (ELF) visualizes the lone pair electrons of =N— groups, confirming their role as Mg-association sites

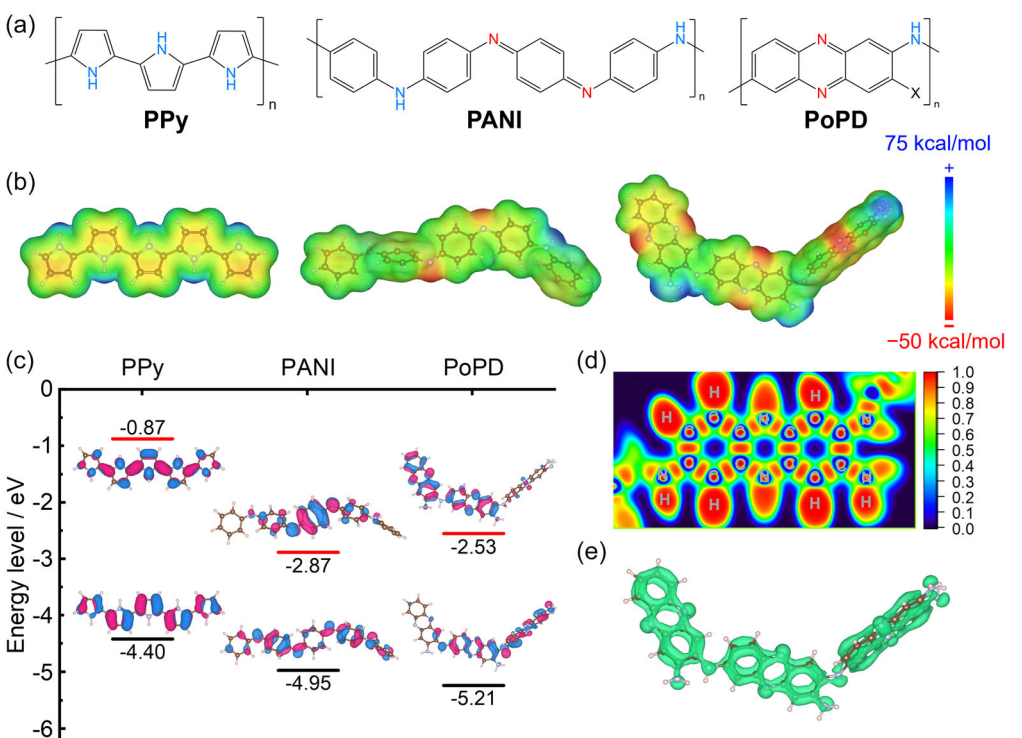


**Figure 1.** a) Chemical structure, b) MESP, c) molecular orbitals of PPy, PANI, and PoPD. d) ELF, and e) LOL- $\pi = 0.4$  isosurface of PoPD.

(Figure 1d). The LOL- $\pi$  isosurfaces of PoPD display nearly continuous distribution across phenazine planes, which is a sign of extended  $\pi$ -conjugation (Figure 1e). The chemical and electronic structure of PoPD facilitates charge delocalization in the Mg-storage reaction, enhancing the reaction reversibility and structural stability.

**Figure 2** presents the structural characterization of PPy, PANI, and PoPD. X-ray diffraction (XRD) patterns (Figure 2a) indicate the amorphous structure of all materials with a broad peak at  $\approx 25^\circ$  attributed to  $\pi-\pi$  stacking interactions, which is usually observed in conjugated polymers.<sup>[19,29]</sup> Elemental analysis (Figure 2b) shows C/N atomic ratios consistent with the chemical structures in Figure 1a. Notably, PoPD exhibits a C/N ratio exceeding 3 (the value for oPD monomer), confirming partial amine group oxidation. Thermogravimetric analysis (TGA) under the N<sub>2</sub> atmosphere shows significantly enhanced thermal stability of PoPD, demonstrating the successful polymerization (Figure 2c). While PoPD displays superior thermal stability, the mass of PANI remains almost unchanged below 400 °C. Polymerization could effectively suppress dissolution in organic electrolytes and improve cycling stability.

The groups of PPy, PANI, and PoPD were characterized by X-ray photoelectron spectroscopy (XPS), Fourier-transform

infrared (FTIR), and Raman spectroscopy. The blue, yellow, and green peaks in N 1s XPS spectra (Figure 2d) are attributed to =N—, —NH—, and —NH<sub>2</sub><sup>+</sup>— groups, respectively. For PPy, the peak of —NH— (399.9 eV) is predominant, while a small amount of protonated —NH<sub>2</sub><sup>+</sup>— (401.8 eV) is caused by the doping during synthesis.<sup>[30]</sup> PANI shows higher —NH— (399.7 eV) content than =N— (398.5 eV) while the corresponding ratio reflects oxidation state variations.<sup>[25]</sup> There is more =N— (399.3 eV) than —NH— (401.0 eV) in PoPD consistent with the expected structural formula (Figure 1a), which implies a higher theoretical Mg-storage capacity. As shown in Figure 2e, FTIR spectra confirm structural features through vibration absorption peaks. The characteristic absorption peaks at 1352 and 1226 cm<sup>-1</sup> correspond to C—N stretching vibrations, while the distinct peak at 1630 cm<sup>-1</sup> arises from C=N stretching vibrations.<sup>[19]</sup> Additional vibrational signatures related to the benzene ring are presented at 1537 cm<sup>-1</sup> (C=C stretching) and 766 cm<sup>-1</sup> (C—H out-of-plane bending), while a broad absorption band centered around 3400 cm<sup>-1</sup> attributed to N—H stretching vibrations.<sup>[31]</sup> PPy and PANI display similar absorption profiles, but C=N vibrations are nearly absent in PPy. Raman spectra (Figure 2f) also confirm these vibrations of groups, though

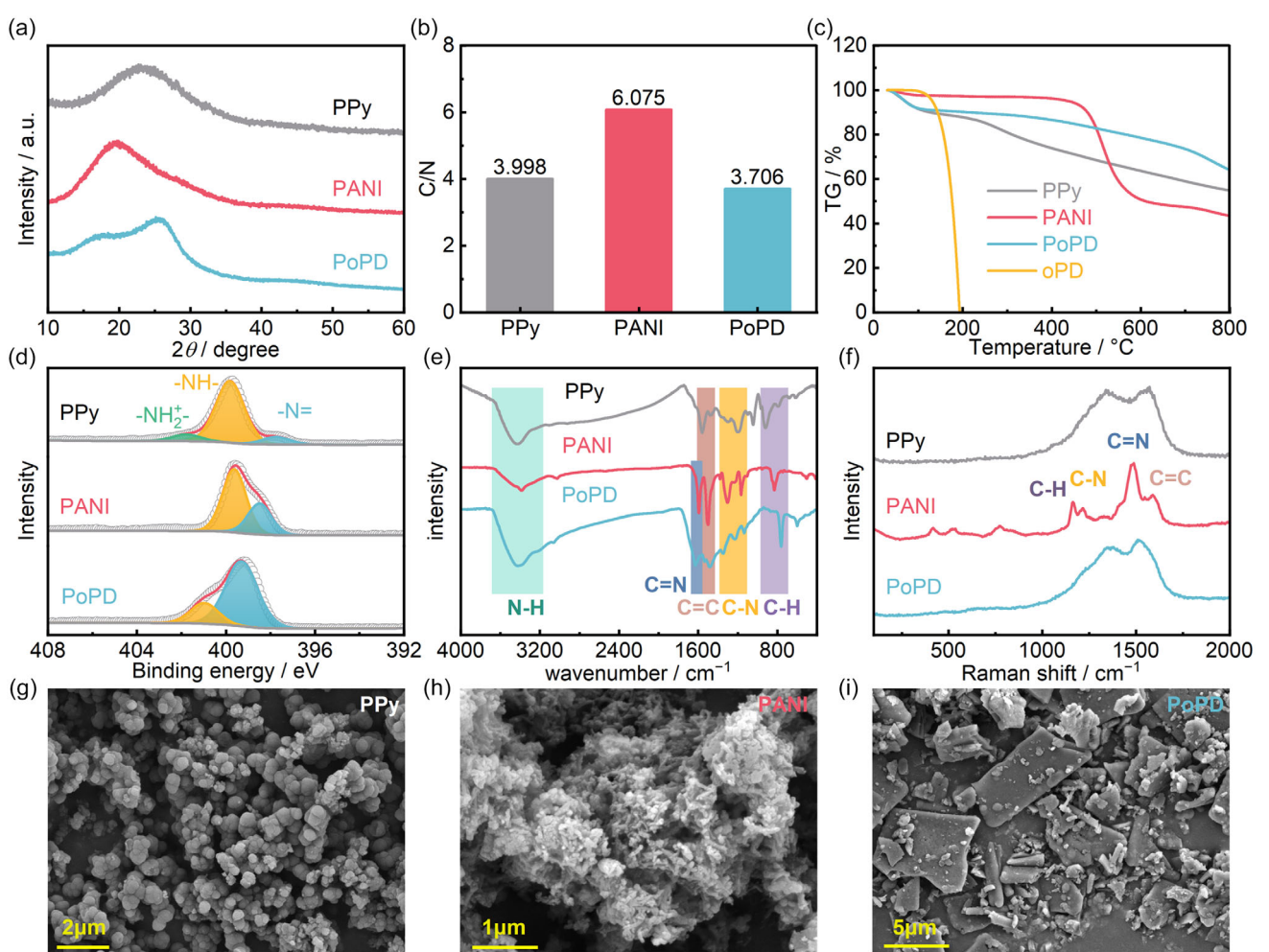


**Figure 2.** a) XRD patterns, b) elements analysis, c) TG analysis, d) N 1s XPS spectra, e) FTIR spectra, f) Raman spectra, and g-i) SEM images of PPy, PANI, and PoPD.

the lower spectra resolution of PPy and PoPD compared to PANI.<sup>[32,33]</sup> Scanning electronic microscope (SEM) images demonstrate the distinct morphological differences among the three polymers. PPy forms agglomerate spherical particles (Figure 2g), PANI consists of short nanofibers (Figure 2h), while PoPD exhibits irregular blocks (Figure 2i).

The Mg-storage performances of PPy, PANI, and PoPD are evaluated and the results are given in Figure 3. In the cyclic voltammetry (CV) tests (Figure 3a), PPy and PoPD exhibit smooth curves without distinct redox peaks. However, PoPD demonstrates a significantly higher current density, indicating higher specific capacity. PANI shows a prominent reduction peak at 1.8 V which is consistent with previous reports. Figure 3b,c and S3, Supporting Information present the cycling performance of PPy, PANI, and PoPD at 100 mA g<sup>-1</sup>. PPy demonstrates negligible Mg-storage capacity within 0.1–2.8 V due to p-type reaction behavior which usually happens at a potential higher than 3.0 V. PANI delivers a capacity of 100 mAh g<sup>-1</sup> with an activation process during initial cycles, showing two discharge voltage plateaus at 2.0 and 1.4 V. As expected, PoPD achieves a high initial capacity of 208 mAh g<sup>-1</sup>, which decreases in early cycles and then gradually recovered, reaching

193 mAh g<sup>-1</sup> after 100 cycles. It is observed that the charge/discharge curves of PoPD lack distinct plateaus, while both dQ/dV plots and CV curves show smooth profiles without redox peaks (Figure S3, Supporting Information). During initial cycles, the charging capacity is higher than discharging with the coulombic efficiency exceeding 100%, which might be caused by the dissolution of the oligomer. As shown in Figure 3d and S4, Supporting Information, the cycling performance of PoPD was also tested at 200 mA g<sup>-1</sup>, which exhibited the same trend and finally achieved a capacity of 172 mAh g<sup>-1</sup>. PoPD also exhibits remarkable rate capability (Figure 3e,f), delivering 79 mAh g<sup>-1</sup> at 5 A g<sup>-1</sup> and 48 mAh g<sup>-1</sup> even at 15 A g<sup>-1</sup>, better than most reported RMB cathodes (Figure 3g).<sup>[34–41]</sup> PoPD shows a lifespan of 1200 cycles with 81.75% capacity retention corresponding to a decay rate of 0.015% per cycle at 15 A g<sup>-1</sup> (Figure 3h). The superior rate capability and cycling stability take advantages of the conjugated structure that enhance reaction reversibility by charge delocalization, while the flexible polymer chains enable rapid Mg<sup>2+</sup> diffusion kinetics.

To explain the capacity evolution (initial decay followed by gradual recovery), morphologies of PoPD electrodes were observed at different states. As shown in Figure S5, Supporting

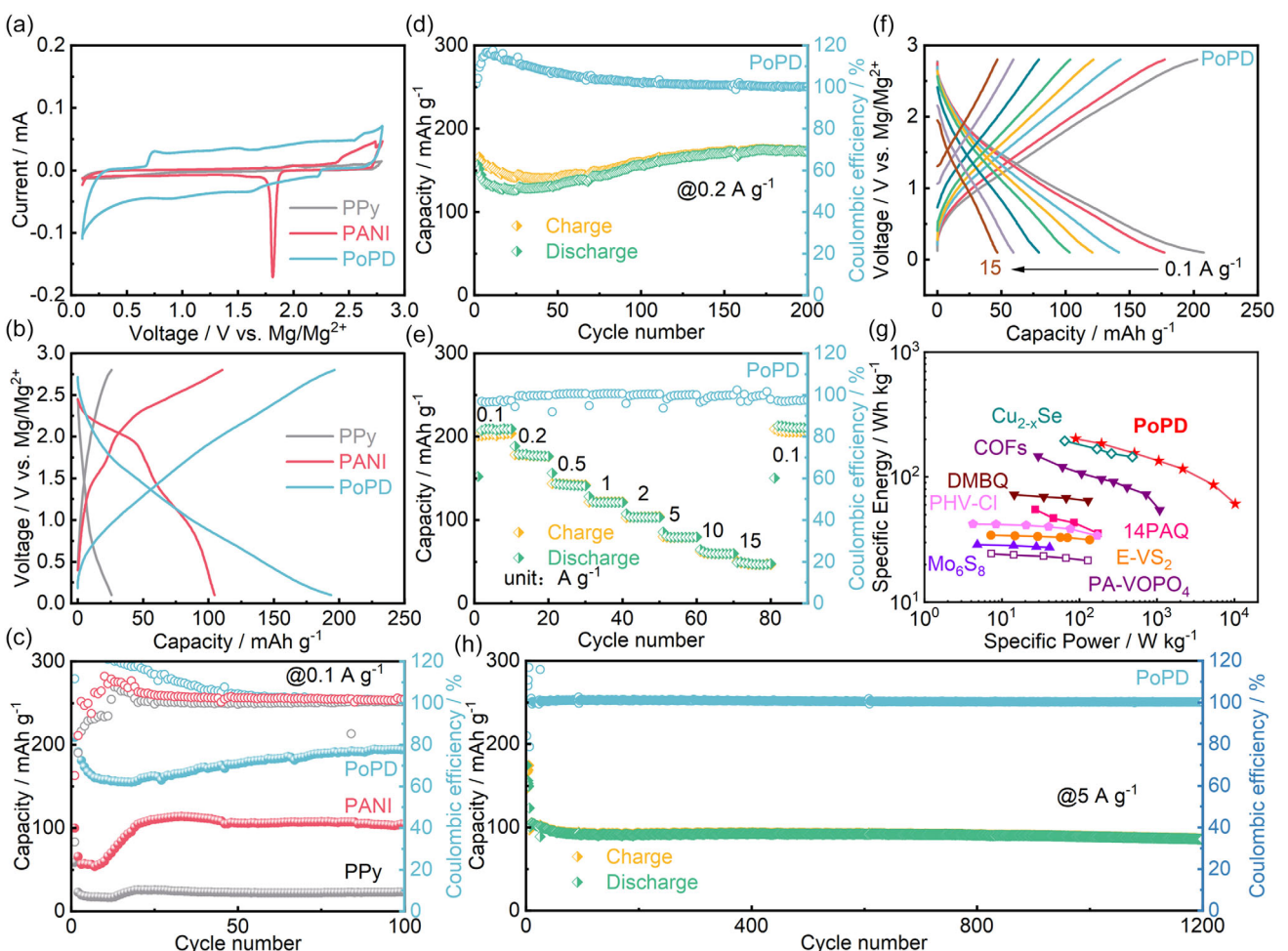


**Figure 3.** a) CV curves, b) typical discharge/charge profiles, c) cycling performance at 0.1 A g<sup>-1</sup> of PPy, PANI, and PoPD, d) cycling performance at 0.2 A g<sup>-1</sup>, e) rate performance, f) associated discharge/charge profiles at various current densities, g) comparison with other RMB cathodes,<sup>[34–41]</sup> and h) long-term cycling performance of PoPD.

Information, significant structural reorganization is observed where the pristine electrode displays large PoPD particles, but the discharged electrodes exhibit particle nanonization. At the same time, the soaking solution of the electrodes showed a dark brown color (Figure S6, Supporting Information), which can be inferred that the dissolution occurred during the discharge process since the original electrodes did not show any change in the DME solution. The electrode surface became flatter with pores filled (Figure S5, Supporting Information) and the electrolyte color became lighter (Figure S6, Supporting Information) after 50 cycles, and the electrolyte turned transparent while the electrode surface was completely covered after 100 cycles. This morphological evolution is strongly related to the cycling performance of PoPD. UV-vis spectra (Figure S7, Supporting Information) of cycled electrolytes show two characteristic absorption peaks at 270 and 415 nm assigned to dissolved PoPD oligomers.<sup>[33]</sup> Thus, the capacity decrease originates from the dissolution of the oligomer during the discharge process, and the electropolymerization occurred in the subsequent cycle resulting in the recovery of capacity.<sup>[42]</sup> PoPD was dissolved in the electrolyte, which may result in the loss of active material and affect battery

performance. Dissolution may expose more active sites or create a more favorable environment for ion transport in the electrolyte and temporarily increase the reaction kinetics.

The Mg-storage mechanism of PoPD was investigated through ex situ XPS and transmission electronic microscope (TEM). In the Mg 1s XPS spectra (Figure 4a), the intensity of Mg increases/decreases during discharge/charge processes, corresponding to the Mg-storage reaction. The residual signal after charging possibly originates from the formed electrode/electrolyte interface and adsorbed Mg electrolyte salt. As shown in Figure 4b, the =N— groups performed as active Mg-storage sites, where Mg coordinated with N atoms during discharge, leading to the corresponding peak of —N—Mg at 398.6 eV.<sup>[28]</sup> The C 1s spectra (Figure 4c) exhibited characteristic  $\pi^*$  satellite peaks at  $\approx$ 293 eV, ascribing to the delocalized electrons in conjugated structures.<sup>[23]</sup> TEM-EDS (Figure 4d) demonstrates simultaneous changes of Mg and Cl contents during cycling, with distinct elemental distribution for discharged/charged electrodes observed in energy dispersive spectrometer (EDS) mappings (Figure 4e,f). It is observed that the peak intensity change of Mg is larger than that of Cl, suggesting PoPD stores both  $Mg^{2+}$  and  $MgCl^-$ .

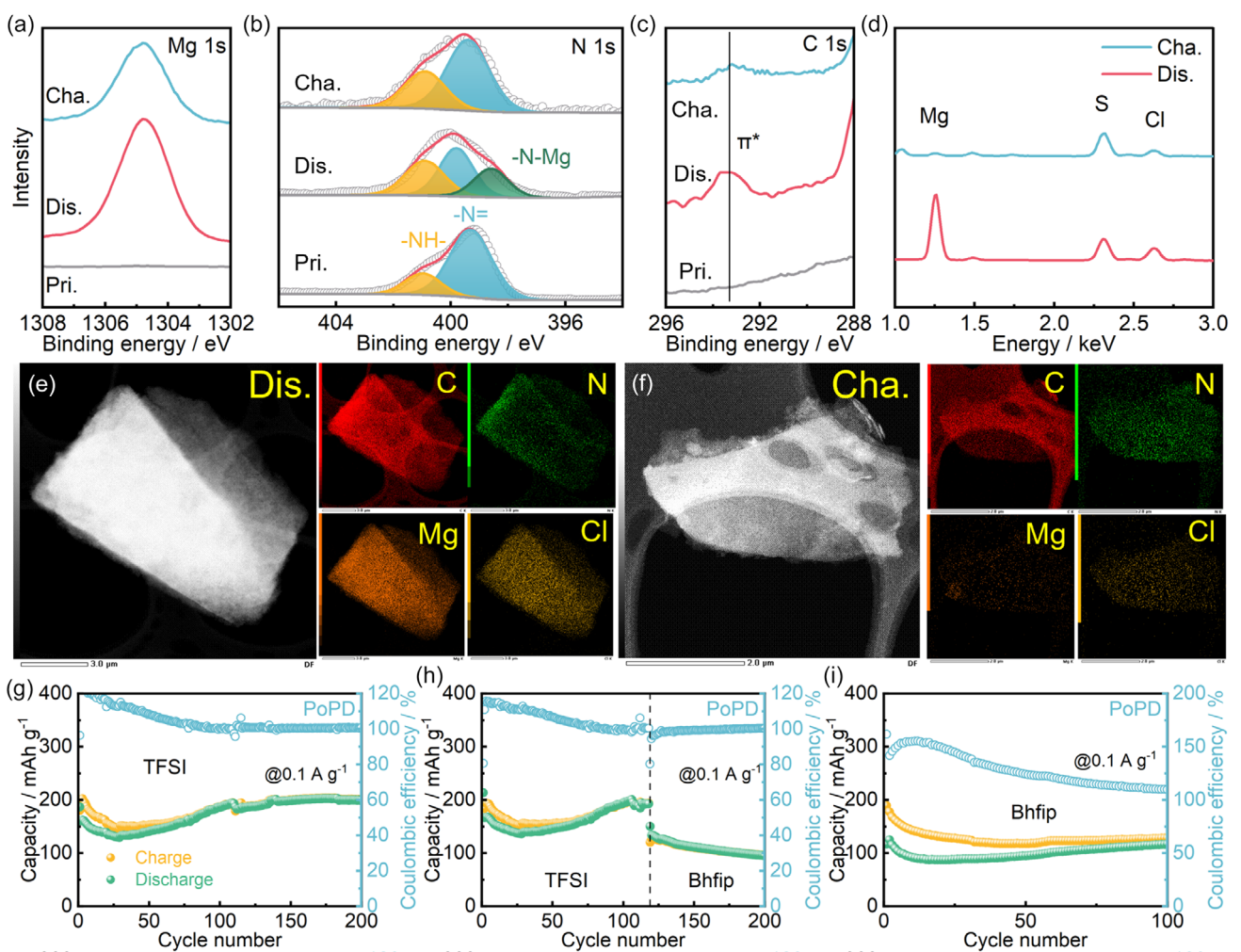


**Figure 4.** Ex situ a) Mg 1s, b) N 1s, c) C 1s XPS spectra of PoPD, d-f) ex situ TEM-EDS of PoPD electrodes. Cycling performances of PoPD in g) chloride-containing, h) electrolyte exchange, and i) chloride-free electrolytes.

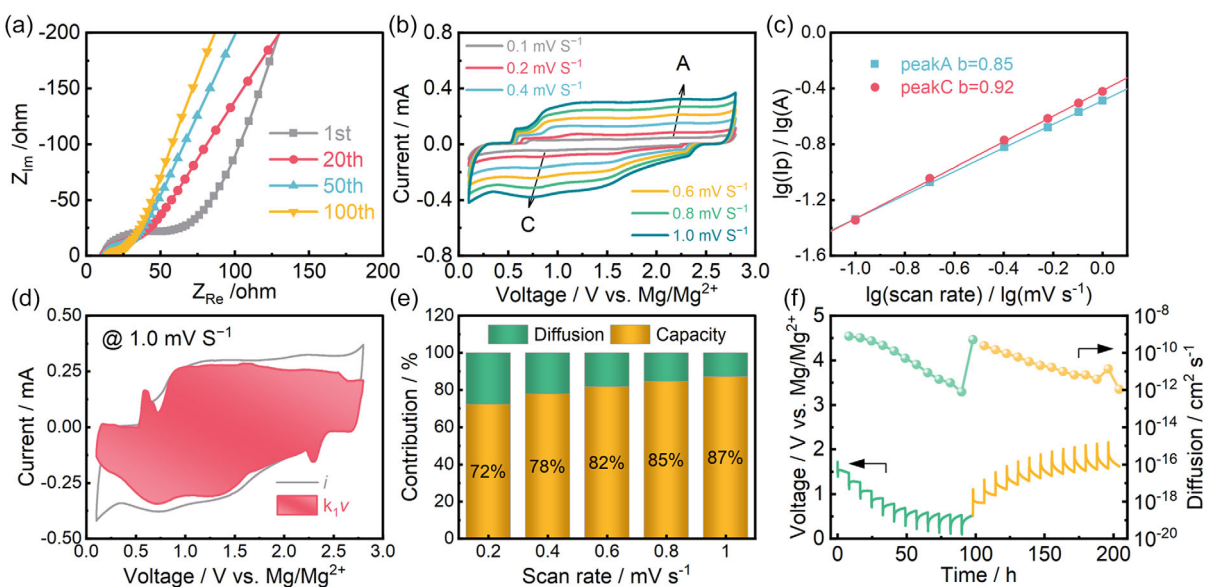


**Figure 5.** a) Impedance Nyquist plots, b) CV curves at various scan rates, c) corresponding  $\log(I_p)$ – $\log(\text{scan rate})$  plots for the redox peaks, d) capacitive contributions at  $1.0 \text{ mV s}^{-1}$  and e) different scan rates, and f) GITT test of PoPD.

Furthermore, the Mg-storage performance of PoPD was evaluated in both chloride-containing and chloride-free electrolytes (Figure 4g–i). PoPD could provide nearly double the capacity in chloride-containing electrolytes (Figure 4g) compared to chloride-free electrolytes (Figure 4i). The capacity significantly decreased when switching from chloride-containing to chloride-free electrolytes (Figure 4h), indicating the costorage of  $\text{Mg}^{2+}$  and  $\text{MgCl}^+$  species. Typically,  $=\text{N}-$  groups undergo single-electron reactions while  $\text{Mg}^{2+}$  coordination with two  $=\text{N}-$  groups from different chains, which may involve higher reaction energy barriers.<sup>[49]</sup> Due to the large phenazine unit of PoPD, the polymer chain is not flexible enough and there is a high resistance to the adjustment of the structure. In contrast,  $\text{MgCl}^+$  could directly associate with only one  $=\text{N}-$  group without requiring complex interchain coordination.<sup>[43]</sup>

Finally, the kinetic performance of PoPD in chloride-containing electrolytes was characterized. Figure 5a provides electrochemical impedance spectroscopy during the cycling, suggesting a continuous reduction of charge transfer resistance ( $R_{ct}$ ).<sup>[44]</sup> In the CV curves at various scan rates (Figure 5b), increased current density and slight redox peak shifts are observed with higher scan rates. The relationship between redox peak current ( $i$ ) and scan rate ( $v$ ) follows the equation  $i = av^b$ , where  $b$ -values were determined through linear fitting of  $\lg i$  and  $\lg v$ .<sup>[45]</sup> The calculated  $b$ -values for peaks A and C were 0.85 and 0.92, respectively indicating high surface-controlled pseudocapacitive behaviors. The diffusion and pseudocapacitive contributions were estimated using the equation  $i(v) = k_1v + k_2v^{1/2}$ , and the results are presented in Figure 5d,e.<sup>[46]</sup> As fitted in Figure 5d, PoPD exhibits 87% pseudocapacitive contribution at  $1.0 \text{ mV s}^{-1}$ , and increases alongside the scan rates. The charge/discharge profiles display none of the distinct plateau owing to the pseudocapacitive controlled Mg-storage mechanism.  $\text{Mg}^{2+}$  diffusion coefficients were further estimated via galvanostatic intermittent titration technique (GITT) (Figure 5f),<sup>[47]</sup>

yielding average values of  $5.16 \times 10^{-11} \text{ cm}^2 \text{ s}^{-1}$  for discharge and  $1.67 \times 10^{-11} \text{ cm}^2 \text{ s}^{-1}$  for charge progress. The rapid  $\text{Mg}^{2+}$  diffusion kinetics in PoPD benefit from weak N–Mg coordination and flexible polymer chain structure.

### 3. Conclusion

In summary, this work developed PoPD as a cathode material for RMBs, demonstrating better performance compared to conventional conductive polymers (PPy and PANI). The imine  $=\text{N}-$  groups in PoPD take the role of active Mg-storage sites, while the extended  $\pi$ -conjugation enhances electron delocalization and structural stability. In chloride-containing electrolytes, PoPD delivers a maximum capacity of  $208 \text{ mAh g}^{-1}$  at  $0.1 \text{ A g}^{-1}$  and 81.75% capacity retention after 1200 cycles at  $5 \text{ A g}^{-1}$ , showing pseudocapacitive-controlled Mg-storage kinetics with rapid  $\text{Mg}^{2+}$  diffusion coefficients ( $10^{-11} \text{ cm}^2 \text{ s}^{-1}$ ). Mechanistic investigation confirms the dual storage capability of PoPD for both  $\text{Mg}^{2+}$  and  $\text{MgCl}^+$  species. This comparative investigation reveals the structure–performance relationship of N-based conjugated polymers, providing valuable insights for developing high-performance organic cathode materials for RMBs.

### 4. Experimental Section

#### Synthesis of PoPD

30 mmol of o-phenylenediamine (oPD) was dissolved in 60 mL of acetic acid (HOAc). A 40 mL solution containing 90 mmol of ammonium persulfate (APS) was then slowly added dropwise to the mixture. After being stirred under reflux for 72 h and cooled to room temperature, the precipitate was separated by vacuum filtration. The

product was subsequently washed sequentially with deionized (DI) water, 0.2 M  $\text{NH}_3\text{H}_2\text{O}$  solution and DI water.

### Synthesis of PPy

30 mmol of pyrrole was dissolved in 300 mL of deionized water under continuous stirring in an ice bath. A 40 mL solution containing 40 mmol of APS was added drop wise into the mixture. Following 1.0 h of stirring in the ice bath, the precipitate was collected via vacuum filtration and thoroughly washed with DI water.

### Synthesis of PANI

25 mmol of aniline was dissolved in 50 mL of 1 M HCl solution under continuous stirring in an ice bath. Separately, 25 mmol of APS was dissolved in 10 mL of DI water, and the resulting solution was added dropwise to the aniline mixture. After 4 h of stirring in the ice bath, the precipitation was separated by vacuum filtration. The obtained material was washed sequentially with DI water, 0.2 M  $\text{NH}_3\text{H}_2\text{O}$  solution, and DI water.

### Structural Characterizations

XRD analysis was conducted using a Rigaku Ultima IV diffractometer to investigate structure characteristics. Molecular vibrations were examined through FTIR and Raman spectroscopy on NICOLET 5700 and HORIBA XploRA PLUS, respectively. Surface chemical states were determined via XPS using an ESCALAB Xi+ instrument. Optical absorption properties were measured with an Agilent Cary 5000 UV-vis spectrophotometer. The morphology was observed by SEM, TESCAN MIRA3 and TEM, JEOL JEM-F200 with EDS attachment. TGA was performed on Mettler-Toledo TGA2 under nitrogen flow conditions. Elemental composition ratios were quantified using an Elementar UNICUBE elemental analyzer (EA).

### Electrochemical Measurements

PoPD electrodes were fabricated by blending active material, Ketjenblack and PTFE with the ratio of 6:3:1 in isopropanol, followed by coating onto carbon paper. After vacuum drying at 70 °C for 24 h, the electrodes were punched into 12 mm discs with a mass loading of  $\approx 1.0 \text{ mg cm}^{-2}$ . CR2032 coin cells were assembled in an argon-filled glovebox ( $\text{H}_2\text{O}/\text{O}_2 < 0.1 \text{ ppm}$ ) using Mg foil anodes and Whatman separators. Electrochemical characteristics including galvanostatic cycling, cyclic voltammetry, and impedance were performed on Land CT3002A battery tester and Ivium-n-Stat electrochemical workstation. Electrochemical tests were performed in the DME electrolyte containing 0.5 M  $\text{Mg}(\text{TFSI})_2$  and 1.0 M  $\text{MgCl}_2$ .  $\text{Mg}[\text{B}(\text{hfip})_4]_2$  electrolyte was synthesized according to the reported article and only used in electrolyte exchange tests.<sup>[6]</sup>

### Computational Details

Theoretical calculations were conducted using Gaussian 16 with the B3LYP functional.<sup>[48,49]</sup> Initial geometry optimizations were performed with def2-SVP basis set and the optimized structures were determined by the absence of imaginary frequencies.<sup>[50]</sup> A larger basis set of def2-TZVP was used for the singlet-point energy calculations. The SMD model was used to take the solvation effect of the electrolyte into consideration.<sup>[7]</sup> To improve the calculation accuracy, DFT-D3 dispersion correction with BJ damping was applied to correct the weak interaction.<sup>[51,52]</sup> Wavefunction analysis was carried out using Multiwfn and visualized by VESTA3.<sup>[53,54]</sup>

### Acknowledgements

This work was financially supported by National Natural Science Foundation of China (no. 22179101). The authors thank the Core Facility of Wuhan University for UV-vis, EA, TG, FTIR, Raman, XPS, and TEM tests. The theoretical calculations in this work were done on the supercomputing system in the Supercomputing Center of Wuhan University.

### Conflict of Interest

The authors declare no conflict of interest.

### Author Contributions

**Donggang Tao:** investigation (lead); writing—original draft (lead). **Yudi Tang:** investigation (supporting). **Hongda Gui:** investigation (supporting). **Yuliang Cao:** conceptualization (equal); software (lead). **Fei Xu:** conceptualization (lead); funding acquisition (lead); writing—review and editing (lead).

### Data Availability Statement

The data that support the findings of this study are available from the corresponding author upon reasonable request.

**Keywords:** cathode materials • imine groups • nitrogen-based active sites • poly(o-phenylenediamine) • rechargeable Mg batteries

- [1] F. Degen, M. Winter, D. Bendig, J. Tübke, *Nat. Energy* **2023**, *8*, 1284.
- [2] M. Rashad, S. D. A. Zaidi, M. Asif, *J. Magn. Alloys* **2020**, *8*, 980.
- [3] J. A. Blázquez, R. R. Maça, O. Leonet, E. Azaceta, A. Mukherjee, Z. Zhao-Karger, Z. Li, A. Kovalevsky, A. Fernández-Barquín, A. R. Mainar, P. Jankowski, L. Rademacher, S. Dey, S. E. Dutton, C. P. Grey, J. Drews, J. Häcker, T. Danner, A. Latz, D. Sotta, M. R. Palacin, J. Martin, J. M. G. Lastra, M. Fichtner, S. Kundu, A. Kraytsberg, Y. Ein-Eli, M. Noked, D. Aurbach, *Energy Environ. Sci.* **2023**, *16*, 1964.
- [4] L. Yang, A. Du, Z. Lv, Z. Zhang, G. Li, *Chem. Eng. J.* **2025**, *506*, 160376.
- [5] T. Wen, H. Xiao, S. Tan, X. Huang, B. Qu, L. Cao, G. Huang, J. Song, J. Wang, A. Tang, J. Yue, F. Pan, *J. Magn. Alloys* **2024**, *12*, 2647.
- [6] S. Li, J. Zhang, S. Zhang, Q. Liu, H. Cheng, L. Fan, W. Zhang, X. Wang, Q. Wu, Y. Lu, *Nat. Energy* **2024**, *9*, 285.
- [7] J. Long, Y. Liu, Z. He, S. Tan, F. Xiong, H. Xu, W. Wang, G. Zhang, Z. Yang, Q. An, *ACS Nano* **2024**, *18*, 15239.
- [8] X. Song, J. Sun, W. Ren, L. Wang, B. Yang, H. Ning, P. Zhang, Z. Caixiang, Z. Tie, X. Zhang, Y. NuLi, Z. Jin, *Angew. Chem. Int. Ed.* **2025**, *64*, e202417450.
- [9] P. Jankowski, Z. Li, Z. Zhao-Karger, T. Diemant, M. Fichtner, T. Vegge, J. M. G. Lastra, *Energy Storage Mater.* **2022**, *45*, 1133.
- [10] D. Zhang, Y. Wang, Y. Yang, Y. Zhang, Y. Zhao, M. Pan, Y. Sun, S. Chen, X. Liu, J. Wang, *Adv. Energy Mater.* **2023**, *13*, 2301795.
- [11] C. Pei, F. Xiong, Y. Yin, Z. Liu, H. Tang, R. Sun, Q. An, L. Mai, *Small* **2021**, *17*, 2004108.
- [12] D. Tao, T. Li, Y. Tang, H. Gui, Y. Cao, F. Xu, *Adv. Funct. Mater.* **2024**, *34*, 202411223.
- [13] D. Wang, Z. Zhang, Y. Hao, H. Jia, X. Shen, B. Qu, G. Huang, X. Zhou, J. Wang, C. Xu, F. Pan, *Adv. Funct. Mater.* **2024**, *34*, 2410406.
- [14] D. Tao, L. Ran, T. Li, Y. Cao, F. Xu, *ACS Nano* **2024**, *18*, 28810.
- [15] Z. Li, J. Häcker, M. Fichtner, Z. Zhao Karger, *Adv. Energy Mater.* **2023**, *13*, 202300682.

- [16] X. He, R. Cheng, X. Sun, H. Xu, Z. Li, F. Sun, Y. Zhan, J. Zou, R. M. Laine, *J. Magn. Alloys* **2023**, *11*, 4359.
- [17] Y. Xiu, A. Mauri, S. Dinda, Y. Pramudya, Z. Ding, T. Diemant, A. Sarkar, L. Wang, Z. Li, W. Wenzel, M. Fichtner, Z. Zhao Karger, *Angew. Chem. Int. Ed.* **2023**, *62*, e202212339.
- [18] X. Ren, D. Tao, S. Cui, T. Li, Y. Cao, F. Xu, *Energy Storage Mater.* **2023**, *63*, 102992.
- [19] Y. Zhao, M. Zhou, X. Zeng, J. Yang, J. Wang, Y. NuLi, *Adv. Funct. Mater.* **2025**, 2423533, <https://doi.org/10.1002/adfm.202423533>.
- [20] Z. Hu, L. Huang, X. Gan, Y. Han, J. Chu, Z. Song, *ACS Appl. Mater. Interfaces* **2024**, *16*, 19014.
- [21] X. Ren, D. Tao, Y. Tang, Y. Cao, F. Xu, *J. Mater. Chem. A* **2023**, *11*, 9955.
- [22] L. Zhu, G. Ding, L. Xie, X. Cao, J. Liu, X. Lei, J. Ma, *Chem. Mater.* **2019**, *31*, 8582.
- [23] S. Cui, T. Li, D. Tao, D. Zhang, Y. Cao, F. Xu, *Energy Storage Mater.* **2024**, *71*, 103672.
- [24] M. Mao, C. Luo, T. P. Pollard, S. Hou, T. Gao, X. Fan, C. Cui, J. Yue, Y. Tong, G. Yang, T. Deng, M. Zhang, J. Ma, L. Suo, O. Borodin, C. Wang, *Angew. Chem. Int. Ed.* **2019**, *58*, 17820.
- [25] Z. Guo, J. Wang, P. Yu, M. Li, L. Huang, Z. Hu, Y. Wang, Z. Song, *Adv. Energy Mater.* **2023**, *13*, 2301520.
- [26] R. H. Sestrem, D. C. Ferreira, R. Landers, M. L. A. Temperini, G. M. Do Nascimento, *Eur. Polym. J.* **2010**, *46*, 484.
- [27] F. Cataldo, *Eur. Polym. J.* **1996**, *32*, 43.
- [28] X. Zhang, G. Li, J. Wang, J. Chu, F. Wang, Z. Hu, Z. Song, *ACS Appl. Mater. Interfaces* **2022**, *14*, 27968.
- [29] Y. Zhang, Y. Li, G. Zhao, L. Han, T. Lu, J. Li, G. Zhu, L. Pan, *J. Mater. Chem. A* **2023**, *11*, 18089.
- [30] S. Padmapriya, V. Sudha, S. Harinipriya, *Int. J. Hydrogen Energy* **2019**, *44*, 6773.
- [31] G. Wei, J. Qiao, X. Li, F. Tao, W. Xue, S. Hu, Z. Luo, J. Yang, *Chem. Eng. J.* **2024**, *496*, 153827.
- [32] M. Trchová, Z. Morávková, M. Bláha, J. Stejskal, *Electrochim. Acta* **2014**, *122*, 28.
- [33] W. Wang, S. Zhang, L. Zhang, R. Wang, Q. Ma, H. Li, J. Hao, T. Zhou, J. Mao, C. Zhang, *Adv. Mater.* **2024**, *36*, 2400642.
- [34] X. Xue, R. Chen, X. Song, A. Tao, W. Yan, W. Kong, Z. Jin, *Adv. Funct. Mater.* **2021**, *31*, 2009394.
- [35] R. Sun, S. Hou, C. Luo, X. Ji, L. Wang, L. Mai, C. Wang, *Nano Lett.* **2020**, *20*, 3880.
- [36] B. Pan, J. Huang, Z. Feng, L. Zeng, M. He, L. Zhang, J. T. Vaughey, M. J. Bedzyk, P. Fenter, Z. Zhang, A. K. Burrell, C. Liao, *Adv. Energy Mater.* **2016**, *6*, 1600140.
- [37] B. Pan, D. Zhou, J. Huang, L. Zhang, A. K. Burrell, J. T. Vaughey, Z. Zhang, C. Liao, *J. Electrochem. Soc.* **2016**, *163*, A580.
- [38] A. B. Ikhe, N. Naveen, K. Sohn, M. Pyo, *Electrochim. Acta* **2018**, *283*, 393.
- [39] P. Jing, H. Lu, W. Yang, Y. Cao, *Electrochim. Acta* **2020**, *330*, 135263.
- [40] P. Saha, P. H. Jampani, M. K. Datta, C. U. Okoli, A. Manivannan, P. N. Kumta, *J. Electrochem. Soc.* **2014**, *161*, A593.
- [41] L. Zhou, Q. Liu, Z. Zhang, K. Zhang, F. Xiong, S. Tan, Q. An, Y. Kang, Z. Zhou, L. Mai, *Adv. Mater.* **2018**, *30*, 1801984.
- [42] S. Sariyer, A. Ghosh, S. N. Dambasan, E. M. Halim, M. El Rhazi, H. Perrot, O. Sel, R. Demir-Cakan, *ACS Appl. Mater. Interfaces* **2022**, *14*, 8508.
- [43] P. Luo, F. Chao, C. Zuo, W. Zhang, F. Xiong, Z. Huang, D. Zhu, G. Yu, W. Zhong, X. Chen, H. Tang, X. Wei, Q. An, *Nano Res.* **2024**, *17*, 6168.
- [44] H. Watanabe, S. Omoto, Y. Hoshi, I. Shitanda, M. Itagaki, *J. Power Sources* **2021**, *507*, 230258.
- [45] Y. Zhang, Y. Zhu, Z. Wang, H. Peng, X. Yang, Y. Cao, C. Du, X. Ma, C. Cao, *Adv. Funct. Mater.* **2021**, *31*, 2104730.
- [46] D. Chao, P. Liang, Z. Chen, L. Bai, H. Shen, X. Liu, X. Xia, Y. Zhao, S. V. Savilov, J. Lin, Z. Shen, *ACS Nano* **2016**, *10*, 10211.
- [47] Z. Shen, L. Cao, C. D. Rahn, C. Wang, *J. Electrochem. Soc.* **2013**, *160*, A1842.
- [48] M. J. Frisch, G. W. Trucks, H. B. Schlegel, G. E. Scuseria, M. A. Robb, J. R. Cheeseman, G. Scalmani, V. Barone, G. A. Petersson, H. Nakatsuji, X. Li, M. Caricato, A. V. Marenich, J. Bloino, B. G. Janesko, R. Gomperts, B. Mennucci, H. P. Hratchian, J. V. Ortiz, A. F. Izmaylov, J. L. Sonnenberg, F. D. Williams, F. Lipparini, F. Egidi, J. Goings, B. Peng, A. Petrone, T. Henderson, D. Ranasinghe, V. G. Zakrzewski, J. Gao, et al., *Gaussian 16 Revision C.01*, Gaussian Inc., Wallingford, CT **2016**.
- [49] A. D. Becke, *J. Chem. Phys.* **1993**, *98*, 5648.
- [50] F. Weigend, R. Ahlrichs, *Phys. Chem. Chem. Phys.* **2005**, *7*, 3297.
- [51] S. Grimme, S. Ehrlich, L. Goerigk, *J. Comput. Chem.* **2011**, *32*, 1456.
- [52] S. Grimme, J. Antony, S. Ehrlich, H. Krieg, *J. Chem. Phys.* **2010**, *132*, 154104.
- [53] K. Momma, F. Izumi, *J. Appl. Crystallogr.* **2011**, *44*, 1272.
- [54] T. Lu, F. Chen, *J. Comput. Chem.* **2012**, *33*, 580.

Manuscript received: March 25, 2025

Revised manuscript received: May 18, 2025

Version of record online: